Boundary layer length scales in convective turbulence

Y.-B. Xin and K.-Q. Xia*
Department of Physics, The Chinese University of Hong Kong, Shatin, New Territories, Hong Kong
(Received 7 October 1996; revised manuscript received 14 May 1997)

Profiles of both the mean value and the standard deviation of the local fluctuating velocity in turbulent convection in water have been directly measured using a light scattering technique. Scaling laws with the Rayleigh number Ra for various boundary layer quantities have been established over the range of Ra from 2.4×10^7 to 1.1×10^{11}, while the variation of the Prandtl number was kept at minimum ($\mathrm{Pr}\simeq 7$). In particular, a new boundary layer length scale is identified from the standard deviation profile, and is found to scale as $\delta_\sigma \sim \mathrm{Ra}^{-0.25}$, whereas the velocity boundary layer thickness $\delta_v \sim \mathrm{Ra}^{-0.16}$. [S1063-651X(97)12309-1]

PACS number(s): 47.27.Te, 42.25.−p, 05.40.+j

As a model system for turbulence studies, Rayleigh-Bénard (RB) convection has attracted lots of interest over the years [1–8], especially after the discovery [9] of the hard turbulence regime in 1987. Much progress, both experimental and theoretical, has been made since then [10–17]. Still, our knowledge about the temperature and the velocity fields near the boundary layers is rather limited. This knowledge has been widely recognized as crucial to the full understanding of turbulent convection [18,19]. In a recent experiment [20], we found scaling properties for several viscous boundary layer quantities measured in a unity-aspect-ratio convection cell. Our results confirm the theoretical predictions of a model by Shraiman and Siggia [12] that the velocity field has a linear profile near cell boundary, and that the thermal boundary layer is nested entirely within the viscous layer. But some of the scaling laws we found do not agree with other predictions of the model. One of these predictions is a relation between the boundary layer shear rate and the Nusselt number (the dimensionless heat flux, which is directly related to the thermal layer thickness), and the other one predicts the crossover between the thermal and the viscous boundary layers at high Rayleigh numbers. Because these theoretical results connect the velocity and the temperature fields in the boundary region, a more detailed experimental investigation aimed at exploring the interplay between the thermal and the viscous boundary layers would certainly be very useful to the understanding of the problem.

In this paper, we report results from direct measurements of the velocity boundary layer properties of turbulent convection in water with the Rayleigh number (Ra) varying from 10^6 to 10^{11}. To achieve such a wide range of Ra, three convection cells of different aspect ratios [$A=$(diameter)/(height)] were used in the experiment. These cells are similar in construction to the aspect-ratio-one cell described in Ref. [20], and we mention only the essential features here. The sidewalls of the cells were Plexiglas cylinders of 19 cm in inner diameter, and their respective heights were 39, 9.4, and 4.3 cm, with the corresponding aspect ratios being 0.5, 2.0, and 4.4. The three cells share the same upper and lower gold-plated copper plates. The temperature of the upper plate was regulated by passing cold water through a cooling chamber fitted on the top of the plate. The lower plate was heated uniformly at a constant rate with an embedded film heater. The temperature difference ΔT between the two plates was measured by two thermistors imbedded in them. The control parameter in the experiment is the Rayleigh number $\mathrm{Ra}=\alpha g L^3 \Delta T/(\nu\kappa)$, with g being the gravitational acceleration, L the height of the cell, and α, ν and κ, respectively, the thermal expansion coefficient, the kinematic viscosity, and the thermal diffusivity of the fluid. The average temperature of the fluid in the convection cell was kept near room temperature during the experiment, and only the temperature difference across the cell was changed. In this way, the variation of the Prandtl number $\mathrm{Pr}=\nu/\kappa$ was kept at minimum ($\mathrm{Pr}\simeq 7$). At the highest Rayleigh number for each cell, the Prandtl number at the top and the bottom plates are $\mathrm{Pr}\simeq 9$ and $\simeq 3$, respectively, which corresponds to a maximum temperature difference $\Delta T\simeq 50$ °C between the two plates. In a separate experiment designed to test the Prandtl number dependence of the various quantities in turbulent convection, we have varied the bulk Pr from 4 to 8 while keeping Ra constant. For this very limited range of Pr, we have found that the characteristic velocity v_m and the shear rate γ_v remain essentially unchanged [21]. Using a movable thermistor probe (size ~ 0.2 mm), we also measured the time-averaged local temperature at different positions along the central axis of the cell. We found that this mean temperature in the center region of the cell (i.e., the region between the top and the bottom thermal boundary layers) is a constant, and its value is halfway between those of the top and the bottom plates for all Rayleigh numbers [22]. From the results of the above two experiments, we conclude that the Boussinesq approximation remains valid in our system [23–25].

In Fig. 1 we show the measured Nusselt number (Nu) as a function of Ra from the aspect ratio $A=0.5$ (squares), 2.0 (triangles), and 4.4 (diamonds) cells, together with those from the $A=1$ cell (circles). It is seen that Nu for the $A=2$, and 4.4 cell showed no apparent dependence on the aspect ratio and has the same amplitude as that from $A=1$ cell. When combined, data from the three cells in the range of Ra from 4.8×10^7 to 1.5×10^{10} give a power-law fit of $\mathrm{Nu}=(0.15\pm0.01)\ \mathrm{Ra}^{0.288\pm0.002}$ (line 2). The measured Nu from $A=0.5$ cell has a different amplitude than those from the

*Electronic address: kxia@phy.cuhk.edu.hk

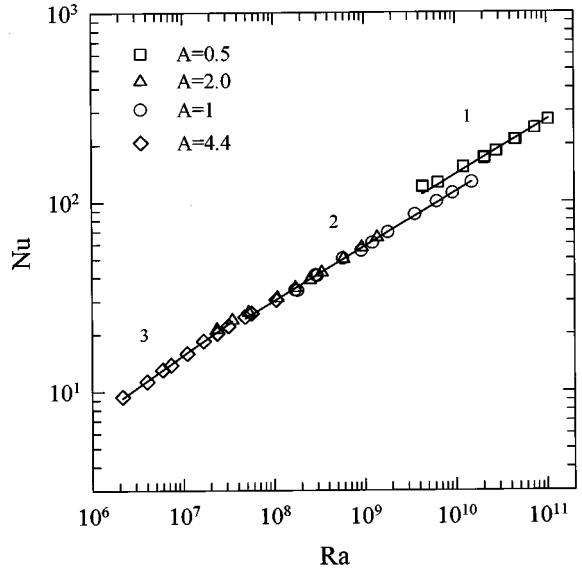

FIG. 1. Nusselt number Nu as a function of the Rayleigh number Ra measured from four different aspect ratio (A) cells as indicated by the different symbols. The solid lines represent power law fits to the corresponding data: $\mathrm{Nu}=0.18\ \mathrm{Ra}^{0.288}$ (line 1), $\mathrm{Nu}=0.15\ \mathrm{Ra}^{0.288}$ (line 2), and $\mathrm{Nu}=0.07\ \mathrm{Ra}^{0.34}$ (line 3).

other cells, and can be described by $\mathrm{Nu}=0.18\ \mathrm{Ra}^{0.288}$ (line 1). The fact that data from different cells have different amplitudes is consistent with the findings made by others that the aspect-ratio dependence of Nu is nonmonotonic [5,26,27]. For Ra below $\sim 3.5\times 10^7$, the measured Nu showed a different Ra dependence than those for higher Rayleigh numbers. This could be taken as the transitional region between the so-called soft- and hard-turbulence. Note that, however, the transition from the ''soft'' to ''hard'' regimes is not sharply defined. As can be seen from Fig. 1, the first few points in line 3 can also be fitted by line 2, but line 3 fits them slightly better (see below for more discussions on the division between the soft and the hard regimes in terms of velocity data). For the limited range of Ra, an attempted power-law fit gives $\mathrm{Nu}=(0.07\pm 0.01)\ \mathrm{Ra}^{0.34\pm 0.01}$ (line 3) for data in the ''soft'' regime.

The light scattering technique of dual-beam incoherent cross-correlation spectroscopy [28] was used to measure the mean value and the standard deviation of the local velocity in the convection cells. In the experiment, two parallel laser beams with a known separation ℓ are shone through the convection cell. The convecting fluid (distilled water) was seeded with neutrally buoyant polymer latex spheres of 0.95 μm in diameter. These particles scatter light and follow the motion of the fluid. The velocity of the seed particles is determined by measuring the time required for the particles to cross the two parallel beams in succession. Experimentally, this transit time, or delay time, is obtained from the cross-correlation function

$$g_c(t)=\frac{\langle I_b(t')I_g(t'+t)\rangle}{\langle I_b(t')\rangle\langle I_g(t')\rangle}=1+\beta G_c(t) \qquad (1)$$

between the scattered intensities, $I_b(t)$ and $I_g(t)$, from the blue and green beams, respectively. In Eq. (1), β ($\leqslant 1$) is an

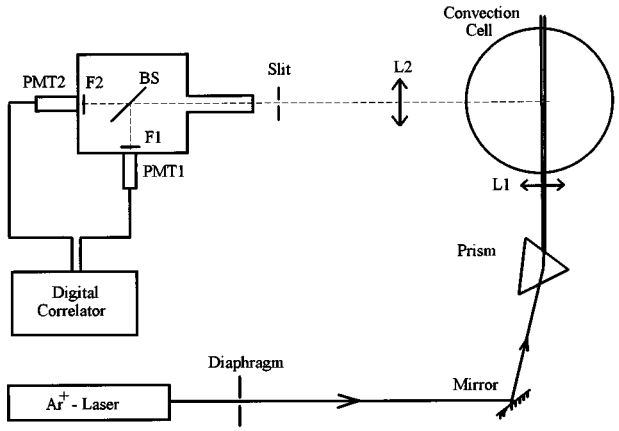

FIG. 2. Schematic diagram of the experimental setup for velocity measurement in a Rayleigh-Bénard convection cell. $L1$ and $L2$ are lenses; BS is a beam splitter; $F1$ and $F2$ are interference filters (center wavelengths 488.0 and 514.5 nm); and PMT1 and PMT2 are photomultiplier tubes.

instrumental constant. Because there is no phase coherence between I_b and I_g, $g_c(t)$ is sensitive only to the scattering amplitude fluctuations produced by the seed particles moving in and out of the laser beams. For a turbulent flow with the probability density function (PDF) $P(v)$ of the local velocity v, assumed to be of a Gaussian form $G_c(t)$ in Eq. (1), has the form [20]

$$G_c(t)=\frac{e^{-(v_0t-\ell)^2/[r_0^2+2(\sigma t)^2]}}{N\sqrt{1+2(\sigma t/r_0)^2}}, \qquad (2)$$

where r_0 is the radius of the beams, N the average number of the particles in the scattering volumes, and v_0 and σ are, respectively, the mean value and the standard deviation of the fluctuating velocity.

Figure 2 shows a schematic diagram of the experimental setup. The argon-ion laser (Coherent Innova-70) was under multiline operation with a wavelength range from 457.9 to 514.5 nm. The prism is so positioned that the exiting point for the color-dispersed beams is at the focal plane of the achromatic lens $L1$ (focal length is equal to 200 mm), this ensures that beams of different colors become parallel to each other after passing through $L1$. The distance between $L1$ and the convection cell is adjusted so the beam waist is at the center of the cell. To determine the separation and the radii of the two dominant intensity beams (wavelength $\lambda=$ 488 and 514.5 nm, respectively) at the center of the convection cell, we placed a small flow cell at the center of a cylindrical Plexiglas tank filled with water. The cylindrical tank has the same diameter and thickness as the sidewall of the convection cell. By running known uniform flows through the flow cell, the beams separation ℓ and their radii r_0 were obtained by fitting the measured cross-correlation function to the formula for uniform flows [28]. The values of the two beam parameters were determined as $\ell=0.30\pm 0.01$ mm and $r_0=0.057\pm 0.005$ mm for the current experiment. In Fig. 2 , the achromatic lens $L2$ (focal length $f=150$ mm) at 90 ° scattering angle serves to project the image of the scattered beams in the cell onto the adjustable slit with 1:1

magnification (i.e., the slit, $L2$, and the scattered beams are in a $2f$-$2f$ configuration). The slit width and the beam diameter together define the scattering volume to be viewed by the photodetectors. The width of the slit was set at 0.3 mm in our experiment. Light passing through the slit fell in a pinhole of 1 mm in diameter. Two photomultiplier tubes (PMT1 and PMT2) were mounted at right angles on a cubic box, which was connected to the pinhole with a 400-mm-long metal tube. This arrangement assured that only the scattered light passing through the slit could be viewed by the two PM tubes. The beam splitter BS at the center of the box had a reflection-to-transmission ratio of 50/50. $F1$ and $F2$ were interference filters with respective center wavelengths 488.0 and 514.5 nm. Both filters had a bandwidth (full width at half maximum) of 1 nm. The pulse trains from the two photomultipliers were fed to a digital correlator (ALV-5000) whose output gives the intensity cross-correlation function $g_c(t)$.

The convection cell sat on a rotational stage which in turn is on top of a three-dimensional translation stage. At the beginning of the velocity measurements, the cell is rotated with respect to the laser beams until a maximum magnitude of velocity is obtained, which corresponds to the laser beams intercepting the large-scale flow perpendicularly. The translation stage has a traveling distance of 200 mm with a resolution of 0.01 mm in the vertical direction, which is adequate for the boundary layer measurements. By fitting Eq. (2) to the measured cross-correlation functions, the mean value v_0 and the standard deviation σ of the local velocity PDF $P(v)$ were obtained. It is found that the measured $G_c(t)$ at different values of Ra and of the distance z from the lower plate can all be well fitted by Eq. (2), indicating that the velocity PDF is indeed of Gaussian form, as was found in the $A=1$ cell [20]. We also measured the velocity with the plane defined by the two laser beams in both horizontal and vertical orientations, and found that the horizontal velocity v_h (simply referred as v hereafter) is the dominant component of the local velocity in the boundary region. This is consistent with what was found in the $A=1$ cell [20], and also with that by others [15]. Profiles of the mean velocity $v(z)$ and the corresponding standard deviation $\sigma(z)$, as functions of z along the central axis of the cell, were then obtained by measuring the correlation function $g_c(t)$ at different height of the parallel beams from the lower plate.

Figure 3 shows a typical $v(z)$ and $\sigma(z)$ measured at $\mathrm{Ra}=1.1\times10^8$ in the $A=2$ cell, where solid dots represent the mean horizontal velocity and the open circles are the corresponding standard deviation. To allow for close examination of the boundary layer region, only the near-wall portion of the profiles are shown in Fig. 3. The complete profiles have the same general features as the mean velocity profile found in the $A=1$ cell [20]. From the measured velocity profile, three boundary layer quantities can be extracted. As shown in Fig. 3, a linear function with zero intercept (nonslip boundary condition) can be well fitted to the initial part of $v(z)$, with the slope of the line being the shear rate γ_v. The thickness δ_v of the viscous boundary layer is defined as the distance at which the extrapolation of the linear part of $v(z)$ equals the maximum velocity v_m (which is the speed of the large scale circulation as discussed in Ref. [20]), or simply $\delta_v=v_m/\gamma_v$. Likewise, a new set of characteristic boundary

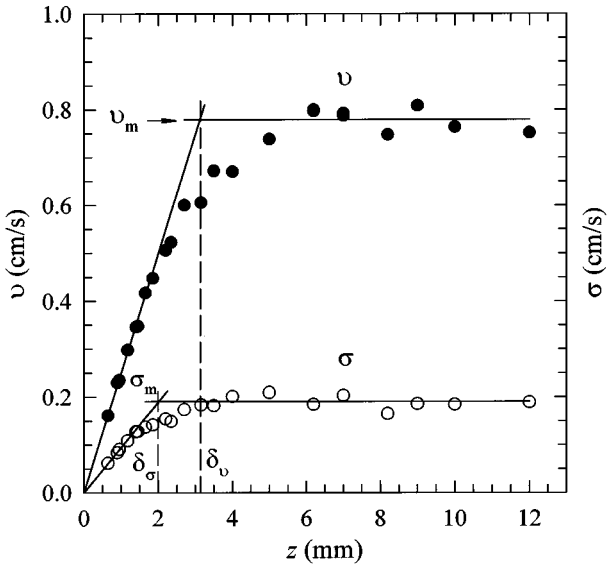

FIG. 3. The mean value v (dots) and the standard deviation σ (circles) of the fluctuating horizontal velocity as functions of the distance z from the lower plate measured at $\mathrm{Ra}=1.1\times10^8$. See text for the meaning of the solid lines and other symbols.

layer quantities γ_σ, σ_m, and δ_σ can be defined and obtained from the standard deviation profile $\sigma(z)$ as depicted in Fig. 3, where the slope for the linear part of $\sigma(z)$ is γ_σ, and $\delta_\sigma=\sigma_m/\gamma_\sigma$. Here, we treat σ, which is a measure of velocity fluctuations, as a certain velocity scale, then γ_σ is a kind of shear rate, and δ_σ is a new viscous length scale in the boundary layer. For the present Ra ($=1.1\times10^8$), the values for the two boundary layer length scales δ_v and δ_σ are found to be 3.1 and 2.0 mm, respectively. As can be seen from Fig. 3, the mean velocity profile starts to deviate from linearity at the standard deviation length scale δ_σ, this is true for all other profiles measured at different Ra. Thus it seems that the nonlinearity of the mean velocity profile is related to the large velocity fluctuations, and the position where v departs from linear behavior may be used to identify the standard deviation length scale. Our measurements also reveal that the velocity profiles $v(z)$ measured from different cells for different Ra in the hard turbulence regime (see below) can all be brought into coincidence, once $v(z)$ is scaled by the characteristic velocity v_m and the distance z is scaled by δ_v. The plot of $v(z)/v_m$ vs z/δ_v is found to remain invariant, and only v_m and δ_v change with Ra. This invariance in functional form is also found for the profiles of the standard deviation $\sigma(z)$, when $\sigma(z)$ is scaled by σ_m and z scaled by δ_σ.

We now discuss the Rayleigh number dependence of the various quantities. In Figs. 4, 5, 6, and 7, we also plot the data from $A=1$ cell [20] for comparison and completeness. Taking the Péclet number Pe ($=v_mL/\kappa$) as the dimensionless characteristic velocity, we plot Pe as a function of Ra in Fig. 4. The different symbols represent data from different aspect-ratio cells: circles ($A=0.5$), triangles ($A=2$), hexagons ($A=4.4$), and squares ($A=1$). It is seen that part of the data ($\mathrm{Ra}\geqslant2\times10^7$) from $A=4.4$ cell and data from $A=1$ cell fall on a single line, a power-law fit to these data gives $\mathrm{Pe}=0.38\ \mathrm{Ra}^{0.50\pm0.01}$ (line 2). Data from $A=0.5$ and $A=2.0$ cells, however, have different amplitudes. Power-law fits to

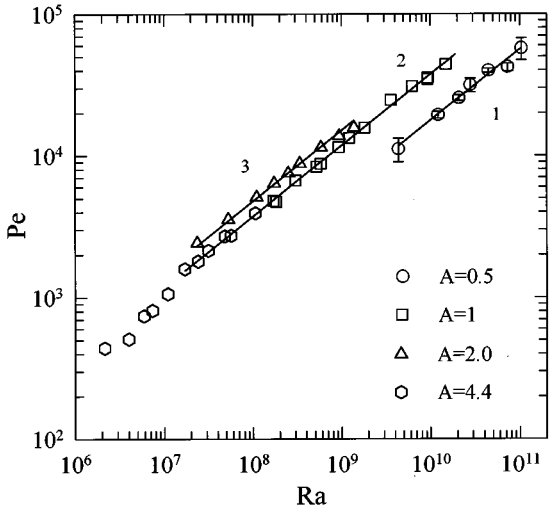

FIG. 4. The Péclet number Pe vs Ra measured from the four different aspect-ratio cells. The solid lines are power-law fits to the measured data: $\mathrm{Pe}=0.18\ \mathrm{Ra}^{0.5}$ (line 1), $\mathrm{Pe}=0.38\ \mathrm{Ra}^{0.5}$ (line 2), and $\mathrm{Pe}=0.48\ \mathrm{Ra}^{0.5}$ (line 3).

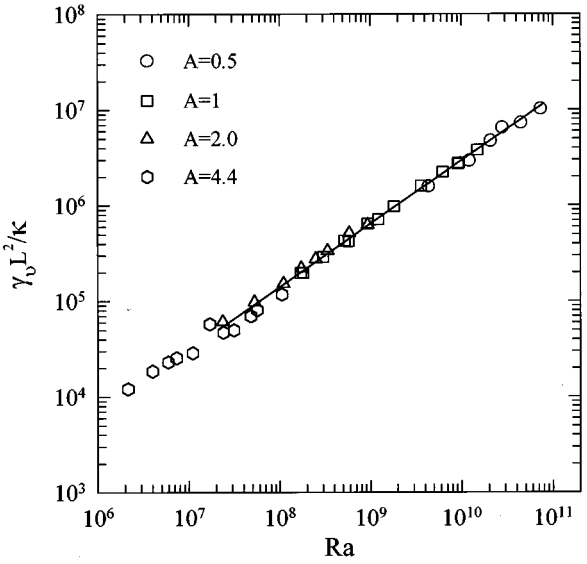

FIG. 6. The dimensionless shear rate $\gamma_v L^2/\kappa$ as a function of Ra measured in the four cells. The solid line is a fit of $\gamma_v L^2/\kappa=0.74\ \mathrm{Ra}^{0.66}$ to data with $\mathrm{Ra}\geqslant 2\times 10^7$.

these give $\mathrm{Pe}=0.18\ \mathrm{Ra}^{0.50\pm 0.04}$ ($A=0.5$, line 1) and $\mathrm{Pe}=0.48\ \mathrm{Ra}^{0.50\pm 0.02}$ ($A=2.0$, line 3). Figure 5 shows the dimensionless maximum standard deviation $\sigma_m L/\kappa$ of the fluctuating velocity versus Ra, the solid line in the figure represents a fit of $\sigma_m L/\kappa=0.11\ \mathrm{Ra}^{0.5}$ for data with $\mathrm{Ra}\geqslant 2\times 10^7$. In Fig. 6 we show the dimensionless shear rate $\gamma_v L^2/\kappa$ as a function of Ra. The solid line there is a fit of $\gamma_v L^2/\kappa=0.74\ \mathrm{Ra}^{0.66}$ for $\mathrm{Ra}\geqslant 2\times 10^7$. Figure 7 is a plot of the dimensionless viscous boundary layer thickness δ_v/L $[=\mathrm{Pe}/(\gamma_v L^2/\kappa)]$ versus Ra. Line 2 is a fit of $\delta_v/L=0.51\ \mathrm{Ra}^{-0.16\pm 0.02}$ to $A=1$ data, while line 3 is a fit to data from $A=2.0$ cell (and a few from $A=4.4$ cell) which gives $\delta_v/L=0.61\ \mathrm{Ra}^{-0.16\pm 0.02}$. Data from the $A=0.5$ cell can also be described by $\delta_v/L=0.3\ \mathrm{Ra}^{-0.16}$ (line 1). It is seen that around $\mathrm{Ra}\simeq 2\times 10^7$ (data from the $A=4.4$ cell), there is an apparent change in the Ra dependence of the respective quantities in Figs. 4, 5, 6, and 7. This Rayleigh number is very close to that of the soft-to-hard turbulence transition ($\mathrm{Ra}=4\times 10^7$) observed in the helium gas experiment conducted in an aspect-ratio-1 cell [9]. We also observed in our experiment that below this Ra the large-scale circulation becomes unstable. Thus $\mathrm{Ra}\simeq 2\times 10^7$ could be identified as the onset Rayleigh number for hard turbulence in our $A=4.4$ cell. Because of the limited number and relatively poorer quality of data, no power-law fits were attempted for this ''soft turbulence'' region. In future studies, it certainly is of interest to have a more systematic investigation of the ''soft turbulent'' state (for example, one thing

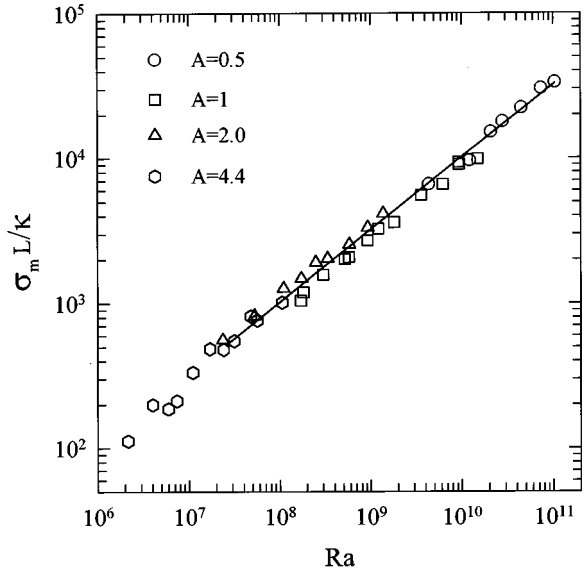

FIG. 5. The scaled maximum standard deviation $\sigma_m L/\kappa$ vs Ra measured in the four cells. The solid line represents the fit of $\sigma_m L/\kappa=0.11\ \mathrm{Ra}^{0.5}$ to data with $\mathrm{Ra}\geqslant 2\times 10^7$.

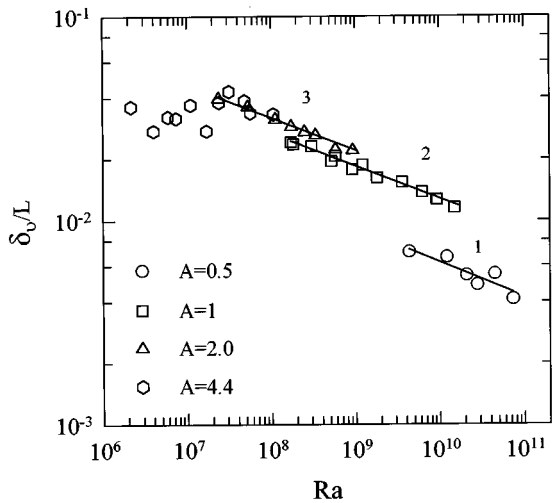

FIG. 7. The scaled viscous boundary layer thickness δ_v/L vs Ra. The different symbols represent data measured from the four aspect ratio cells. The solid lines are power-law fits to the corresponding data: $\delta_v/L=0.3\ \mathrm{Ra}^{-0.16}$ (line 1), $\delta_v/L=0.51\ \mathrm{Ra}^{-0.16}$ (line 2), and $\delta_v/L=0.61\ \mathrm{Ra}^{-0.16}$ (line 3).

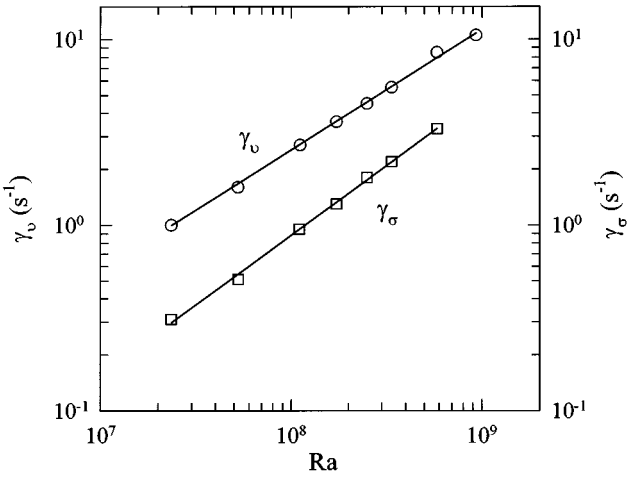

FIG. 8. Boundary layer shear rates γ_v (circles) for the mean velocity and γ_σ (squares) for the standard deviation as functions of Ra. Power law fits to the measured data give $\gamma_v=(1.8\pm0.9)\times10^{-5}$ $\mathrm{Ra}^{0.66\pm0.02}\,\mathrm{s}^{-1}$, and $\gamma_\sigma=(9\pm2)\times10^{-7}$ $\mathrm{Ra}^{0.75\pm0.02}\,\mathrm{s}^{-1}$.

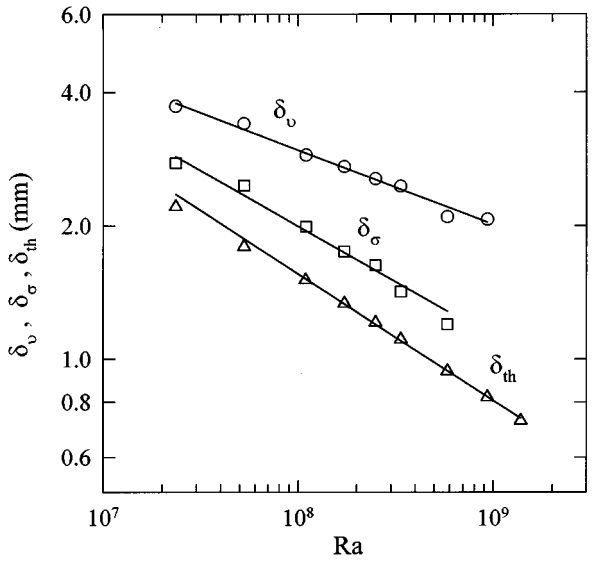

FIG. 9. Measured velocity boundary layer length scales δ_v (circles) and δ_σ (squares), and the thermal boundary layer thickness δ_{th} (triangles) vs Ra. The solid lines represent power-law fits $\delta_v=(66\pm9)$ $\mathrm{Ra}^{-(0.16\pm0.02)}$ mm, $\delta_\sigma=(2.0\pm0.6)\times10^2$ $\mathrm{Ra}^{-(0.25\pm0.02)}$ mm, and $\delta_{\mathrm{th}}=(3.1\pm0.2)\times10^2$ $\mathrm{Ra}^{-(0.288\pm0.002)}$ mm.

would be to ascertain the apparent level-off of the viscous layer thickness in Fig. 7 below $\mathrm{Ra}\simeq2\times10^7$).

One thing we have noticed from Figs. 4, 5, 6, and 7 is that the scaled shear rate $\gamma L^2/\kappa$ for different aspect ratio (A) cells fall almost perfectly on a single line, while the scaled maximum standard deviation $\sigma_m L/\kappa$ for different cells fall within a narrow band; but for the Péclet number, its amplitude seems to have a nonmonotonic dependence on A, and the difference is beyond experimental uncertainties (the scaled viscous layer thickness δ_v/L is simply the ratio of Pe to $\gamma L^2/\kappa$). This behavior of Pe has also been observed by Wu and Libchaber in their study of the aspect ratio dependence of turbulent convection [27]. We do not know the exact reasons for this. We suspect that it might have to do with the fact that the shear rate is essentially a boundary layer property, and σ_m is a measure of the velocity fluctuations, while Pe ($=v_m L/\kappa$) is an overall velocity scale in the convection cell. As was discussed earlier, the Nusselt number (which is a measure of the overall heat transport in the cell) also has a nonmonotonic dependence on A. It has been observed by us [21], and others [27], that the aspect ratio affects the overall flow patterns in a convection cell. Thus the above may be a manifestation that overall flow pattern has more influence on global properties than it is on local properties of the convective flow.

In Ref. [20], we established power laws for the characteristic velocity v_m, the maximum standard deviation σ_m, the shear rate γ_v, and the viscous boundary layer thickness δ_v from measurements in the aspect-ratio-1 cell where Ra varied from 2×10^8 to 2×10^{10}. The results shown in Figs. 4, 5, 6, and 7 tell us that these power laws hold for different aspect-ratio cells in the hard turbulence regime for nearly four decades of Ra ($\sim2.4\times10^7$ to $\sim1\times10^{11}$). We concentrate below on the scaling behavior of the new boundary layer quantities extracted from the standard deviation profiles.

The squares in Fig. 8 represent the gradient (or ''shear rate'') for the standard deviation, γ_σ, as a function of Ra measured in the $A=2$ cell. The solid line is a fit of $\gamma_\sigma=(9\pm2)\times10^{-7}$ $\mathrm{Ra}^{0.75\pm0.02}\,\mathrm{s}^{-1}$ to the data. For comparison, we plot here also the corresponding shear rate for the mean velocity γ_v (circles). The upper solid line represents the power law fit $\gamma_v=(1.8\pm0.9)\times10^{-5}$ $\mathrm{Ra}^{0.66\pm0.02}\,\mathrm{s}^{-1}$. Thus γ_σ is seen to have a scaling behavior different from that of γ_v. If we pick the thermal boundary layer thickness δ_{th} as a typical length scale within the viscous boundary layer, and using the relation $\delta_{\mathrm{th}}=L/2Nu$ [15], then the typical velocity inside viscous layer can be estimated as $v_{\mathrm{th}}=\gamma_v\delta_{\mathrm{th}}\sim\mathrm{Ra}^{0.37}$, and the corresponding standard deviation $\sigma_{\mathrm{th}}=\gamma_\sigma\delta_{\mathrm{th}}\sim\mathrm{Ra}^{0.46}$. Thus the velocity fluctuation inside the viscous layer is seen to grow faster with Ra than the mean velocity, in contrast to the situation just outside the boundary layer, where both v_m and σ_m scale as $\mathrm{Ra}^{0.5}$. If the ratio σ/v can be taken as a measure for the level of turbulence, then the above implies that σ_m/v_m is independent of Ra, while $\sigma_{\mathrm{th}}/v_{\mathrm{th}}$ increases with Ra. This means that the velocity boundary layer will become more turbulent than the central region at higher Rayleigh number. In a recent model, it was predicted that $\mathrm{Nu}\sim\gamma^{1/3}$ [12], which implies that the heat flux is carried entirely by the large-scale flow with the thermal plumes playing a negligible role. With the measured $\gamma_v(\mathrm{Ra})$ and $\mathrm{Nu}(\mathrm{Ra})$, we obtain $\mathrm{Nu}\sim\gamma_v^{0.44}$ which is quite different from what the theory predicts. If we take the view that it is the velocity fluctuation rather than the mean velocity that is relevant in determining the statistical properties of turbulence, then we should compare our measured $\gamma_\sigma(\mathrm{Ra})$ with the theoretical $\gamma(\mathrm{Ra})$. Similar to the above, we find $\mathrm{Nu}\sim\gamma_\sigma^{0.38\pm0.01}$, which is still quite different from, though closer to, the theoretical prediction. This means that the large-scale flow is not able to carry all the heat flux across the cell, and the contribution by thermal plumes cannot be neglected.

We now present and discuss the scaling behavior of the various boundary layer length scales. Figure 9 shows the length scales $\delta_v(\mathrm{Ra})$ (circles) and $\delta_\sigma(\mathrm{Ra})$ (squares) ob-

tained, respectively, from the mean velocity and the standard deviation profiles, and the thermal boundary layer thickness δ_{th}(Ra) (triangles). Again, for clarity, only data from $A=2$ cell are shown. Note that the absolute length scales are plotted here rather than the dimensionless lengths. The solid lines in Fig. 9 are power-law fits to the respective data, i.e., $\delta_v=(66\pm9)\ \mathrm{Ra}^{-(0.16\pm0.02)}$ mm, $\delta_\sigma=(2.0\pm0.6)\times10^2\ \mathrm{Ra}^{-(0.25\pm0.02)}$ mm, and $\delta_{th}=(3.1\pm0.2)\times10^2\ \mathrm{Ra}^{-(0.288\pm0.002)}$ mm (converted from Nu using $\delta_{th}=L/(2\,\mathrm{Nu})$, the fitting is for data from $A=1$, 2, and 4.4 cells in the hard turbulence regime, the data points shown here are those from $A=2$ cell only). It is seen from Fig. 9 that the largest velocity fluctuations occur inside the viscous boundary layer, and the difference between the two length scales δ_v and δ_σ diverges with Ra. From temperature measurements in water and gas [15,18], and in mercury [29], it has been found that the maximum of the rms temperature fluctuations occur approximately at the edge of the thermal boundary layer, and thus quite different than the relation between δ_v and δ_σ found above. The fact that δ_σ has a scaling exponent that is intermediate those of δ_v and δ_{th} suggests it is the length scale over which the temperature and velocity fields are coupled to each other, in the sense that their fluctuations are ''feeding each other.'' Thus δ_σ could be used as an alternative measure for the temperature boundary layer thickness, as was previously conjectured in Ref. [15]. However, from Fig. 9, it is seen that the two have slightly different exponents and also differ in amplitudes. Thus the association of the two length scales need to be further verified. For now, we view δ_σ as a new and independent length scale in the problem. It is also evident from Fig. 9 that, whether we choose δ_v or δ_σ as the relevant length scale for the viscous layer, the thermal and viscous boundary layers would not crossover at higher Ra if the current trend for these quantities continues. This is consistent with the result from a two-dimensional simulation study of turbulent convection [30].

In summary, our measurements have revealed scaling laws for boundary layer quantities from the standard deviation profile, and extended those from the mean velocity profile, over a range of Ra that span from 10^7 to 10^{11}. We have shown that the mean value and the standard deviation of the fluctuating velocity have the same scaling behavior outside the boundary region but have quite different behavior inside the boundary layer where large temperature gradient exists. The scaling behavior of the three boundary layer length scales suggest that the thermal boundary layer have a stronger effect on velocity fluctuations than it has on the mean velocity.

ACKNOWLEDGMENTS

We thank P. Tong, E. S. C. Ching, and B. I. Shraiman for helpful discussions. This work was supported by the Hong Kong Research Grants Council under Grant No. 319/96P.

[1] W. V. R. Malkus, Proc. R. Soc. London, Ser. A **225**, 180 (1954); **225**, 196 (1954).
[2] A. A. Townsend, J. Fluid Mech. **5**, 209 (1959).
[3] L. N. Howard, in *Proceedings of the 11th International Congress of Applied Mechanics, Munich* (Springer-Verlag, Berlin, 1966), p. 1109.
[4] R. J. Goldstein and T. Y. Chu, Prog. Heat Mass Trans. **2**, 55 (1969).
[5] T. Y. Chu and R. J. Goldstein, J. Fluid Mech. **60**, 141 (1973).
[6] D. C. Threlfall, J. Fluid Mech. **67**, 17 (1975).
[7] H. Tanaka and H. Miyata, Int. J. Heat Mass Transf. **23**, 1273 (1980).
[8] R. Krishnamurti and L. N. Howard, Proc. Natl. Acad. Sci. USA **78**, 1981 (1981).
[9] F. Heslot, B. Castaing, and A. Libchaber, Phys. Rev. A **36**, 5870 (1987).
[10] B. Castaing, G. Gunaratue, F. Heslot, L. P. Kadanoff, A. Libchaber, S. Thomae, X.-Z. Wu, S. Zaleski, and G. Zanetti, J. Fluid Mech. **204**, 1 (1989).
[11] M. Sano, X.-Z. Wu, and A. Libchaber, Phys. Rev. A **40**, 6421 (1989).
[12] B. I. Shraiman and E. D. Siggia, Phys. Rev. A **42**, 3650 (1990).
[13] T. H. Solomon and J. P. Gollub, Phys. Rev. Lett. **64**, 2382 (1990); Phys. Rev. A **43**, 6683 (1991).
[14] P. Tong and Y. Shen, Phys. Rev. Lett. **69**, 2066 (1992).
[15] A. Tilgner, A. Belmonte, and A. Libchaber, Phys. Rev. E **47**, R2253 (1993).
[16] F. Chilla, S. Ciliberto, and C. Innocenti, Europhys. Lett. **22**, 681 (1993).
[17] Y. Shen, K.-Q. Xia, and P. Tong, Phys. Rev. Lett. **75**, 437 (1995).
[18] A. Belmonte, A. Tilgner, and A. Libchaber, Phys. Rev. Lett. **70**, 4067 (1993); Phys. Rev. E **50**, 269 (1994).
[19] E. D. Siggia, Annu. Rev. Fluid Mech. **26**, 137 (1994), and references therein.
[20] Y.-B. Xin, K.-Q. Xia, and P. Tong, Phys. Rev. Lett. **77**, 1266 (1996).
[21] Y.-B. Xin, Ph.D. thesis, The Chinese University of Hong Kong, 1996 (unpublished).
[22] S.-L. Lui and K.-Q. Xia (unpublished).
[23] D. J. Tritton, *Physical Fluid Dynamics*, 2nd ed. (Clarendon, Oxford, 1988).
[24] X.-Z. Wu and A. Libchaber, Phys. Rev. A **43**, 2833 (1991).
[25] J. Zhang, S. Childress, and A. Libchaber, Phys. Fluids **9**, 1034 (1997).
[26] J. W. Deardorff and J. E. Willis, J. Fluid Mech. **23**, 337 (1965).
[27] X.-Z. Wu and A. Libchaber, Phys. Rev. A **45**, 842 (1992).
[28] K.-Q. Xia, Y.-B. Xin, and P. Tong, J. Opt. Soc. Am. A **12**, 1571 (1995).
[29] T. Takeshita, T. Segawa, J. A. Glazier, and M. Sano, Phys. Rev. Lett. **76**, 1465 (1996).
[30] J. Werne, Phys. Rev. E **48**, 1020 (1993).